

Nanoparticles Accumulate in the Female Reproductive System during Ovulation Affecting Cancer Treatment and Fertility

Maria Poley,[#] Patricia Mora-Raimundo,[#] Yael Shammai, Maya Kaduri, Lilach Koren, Omer Adir, Jeny Shklover, Janna Shainsky-Roitman, Srinivas Ramishetti, Francis Man, Rafael T. M. de Rosales, Assaf Zinger,^{*} Dan Peer, Irit Ben-Aharon, and Avi Schroeder^{*}



Cite This: <https://doi.org/10.1021/acsnano.1c07237>



Read Online

ACCESS |



Metrics & More



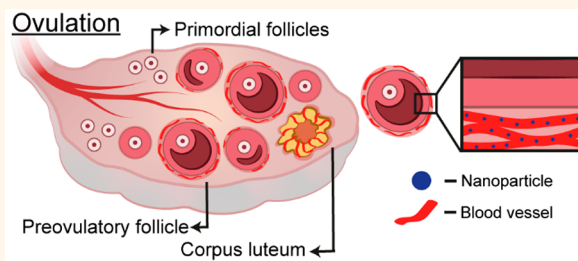
Article Recommendations



Supporting Information

ABSTRACT: Throughout the female menstrual cycle, physiological changes occur that affect the biodistribution of nanoparticles within the reproductive system. We demonstrate a 2-fold increase in nanoparticle accumulation in murine ovaries and uterus during ovulation, compared to the nonovulatory stage, following intravenous administration. This biodistribution pattern had positive or negative effects when drug-loaded nanoparticles, sized 100 nm or smaller, were used to treat different cancers. For example, treating ovarian cancer with nanomedicines during mouse ovulation resulted in higher drug accumulation in the ovaries, improving therapeutic efficacy. Conversely, treating breast cancer during ovulation, led to reduced therapeutic efficacy, due to enhanced nanoparticle accumulation in the reproductive system rather than at the tumor site. Moreover, chemotherapeutic nanoparticles administered during ovulation increased ovarian toxicity and decreased fertility compared to the free drug. The menstrual cycle should be accounted for when designing and implementing nanomedicines for females.

KEYWORDS: gender medicine, gold nanoparticles, liposome, mRNA LNP, fertility, ovarian cancer, breast cancer



The female reproductive system undergoes cyclic hormonal and physiological changes that lead to ovulation.¹ For female mice, the estrous cycle (the equivalent of the human female menstrual cycle) is divided into four stages: diestrus (nonovulatory), proestrus, estrus, and metestrus.² During the preovulatory proestrus stage, angiogenesis and perfusion within the reproductive system support oocyte maturation, followed by ovulation and estrus (Figure 1a,b, left).^{1,3} At ovulation, the oocyte ruptures from the ovarian follicle and is transformed into the highly vascular corpus luteum. Ending the cycle, the metestrus stage, the corpus luteum is absorbed back into normal stromal ovarian cells. As a result, the corpus luteum undergoes exceptionally fast tissue growth and angiogenesis.⁴ Angiogenesis in the ovaries and the uterus is accompanied by high levels of vascular endothelial growth factor (VEGF) secretion, leading to enhanced permeability of blood vessels.⁵ Thus, we and others^{6,7} hypothesized that the cyclic nature of an increase in leaky blood vessels within the reproductive system may affect nanoparticle biodistribution during different stages of the menstrual cycle (Figure 1a,b, right).

Nanotechnologies are important clinical tools, allowing accurate diagnosis and therapy.^{8–11} Nanoparticles can be composed of organic and inorganic materials and carry various cargoes including small molecules, proteins, and nucleic acids. Several nanomedicines are approved clinically for treating breast and ovarian cancer, such as 100 nm liposomal doxorubicin and 110 nm albumin-bound paclitaxel particles.^{12,13} Medicines distributing to the female reproductive system can improve the efficacy of localized treatments or pose a threat to fertility by inducing ovarian toxicity and subsequent ovarian failure.^{14–17}

Global regulatory guidance, due to failed clinical implementation of drugs used by females, has directed attention toward sex-specific medicine practice (previously known as “gender medicine”).¹⁸ Foci include the study of female-specific administration routes, such as vaginal delivery,^{19–21} and

Received: August 20, 2021

Accepted: March 14, 2022



ACS Publications

© XXXX American Chemical Society

A

<https://doi.org/10.1021/acsnano.1c07237>
ACS Nano XXXX, XXX, XXX–XXX

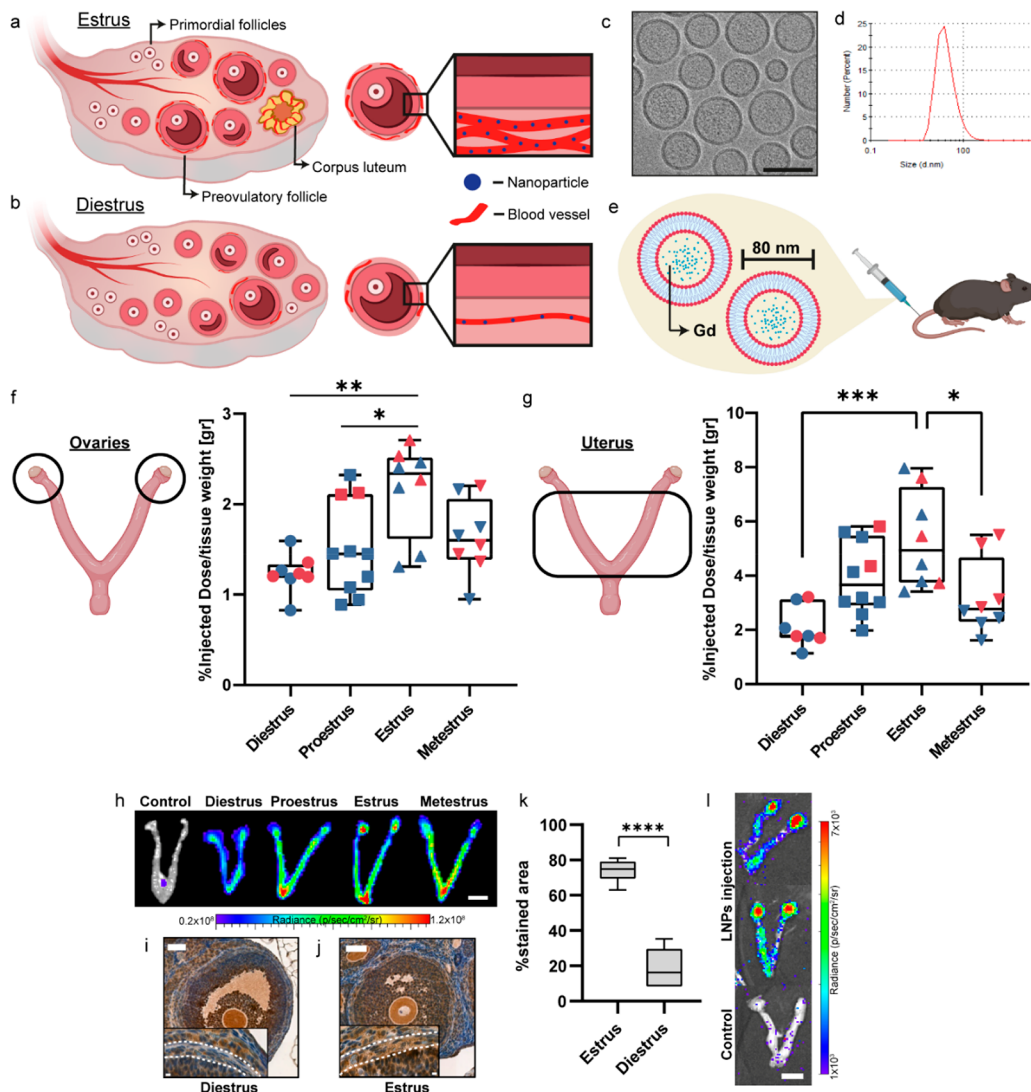


Figure 1. Biodistribution of nanoparticles to the reproductive system during the female mouse menstrual cycle. During the estrus stage there is increased blood supply to the ovary to support preovulatory follicles. After ovulation, a dense blood network termed the corpus luteum is observed. A higher density of blood vessels around the follicle results in a higher accumulation of nanoparticles (blue) in the reproductive system (a). Contrarily, there are fewer blood vessels in the ovary and around the follicles specifically during the diestrus stage (b). 80 nm Gd-loaded PEGylated liposomes (Gd-lipo) were imaged using cryo-TEM (c, scale bar 100 nm) and sized using dynamic light scattering (DLS) (d). Gd-lipo were injected intravenously (i.v.) to female mice at different stages of the menstrual cycle (e). Nanoparticle accumulation 24 h postadministration was quantified using elemental analysis for Gd or by mRNA expression. Results are shown as the injected %Gd normalized to the organ weight. 1.8-fold more liposomes reached the ovaries at the estrus stage ($n = 8$) compared to the diestrus stage ($n = 8$, red and blue represent two independent experiments) (f). 2.5-fold more liposomes reached the uterus at the estrus stage ($n = 7$) (g). *Ex vivo* fluorescent images of the female murine reproductive system 24 h post i.v. injection of 80 nm Cy5-labeled liposomes during the different ovulation stages (h, scale bar 0.5 cm). Blood vessel density was evaluated using anti-CD31 immunohistochemistry staining at diestrus (i) and estrus stages (j) (scale bar 100 μm) and was quantified as the percentage of stained area compared to a control stained only with secondary Ab (k). Expression of firefly luciferase in the ovaries during estrus, 24 h post i.v. injection of lipid nanoparticles loaded with firefly luciferase mRNA. The bottom image is a control without nanoparticles injection (scale bar 0.5 cm) (l). Results are shown as mean \pm SEM. One-way ANOVA and Tukey's t test were used for statistical analysis of f and g, unpaired two-tail t test was used for statistical analysis of k. * $p < 0.05$, ** $p < 0.01$, *** $p < 0.001$, **** $p < 0.0001$. Illustrations e, f, and g were made using BioRender.

evaluating differences in pharmacokinetic parameters of clinically approved small-molecule medicines and nanomedicines.²² For example, it was shown that PEGylated liposomal doxorubicin has a slower overall clearance rate in females compared to males.²² The reason behind this sex-related difference is yet to be determined; however, longer residence time in the body impacts efficacy, dosing regimens, and drug tolerability.²³ Preclinical characterization of sex-dependent nanoparticle biodistribution and pharmacokinetics is therefore

an essential step in developing nanocarriers, especially given the wide variety of medicinal nanoparticle types and applications.^{24–26}

Here, we study how the female menstrual cycle affects the accumulation of nanoparticles in the reproductive system. We then explore how the efficacy of nanomedicines in cancer treatment is affected by the menstrual cycle stages in mice, as well as the effect chemotherapy-loaded nanoparticles have on female fertility.

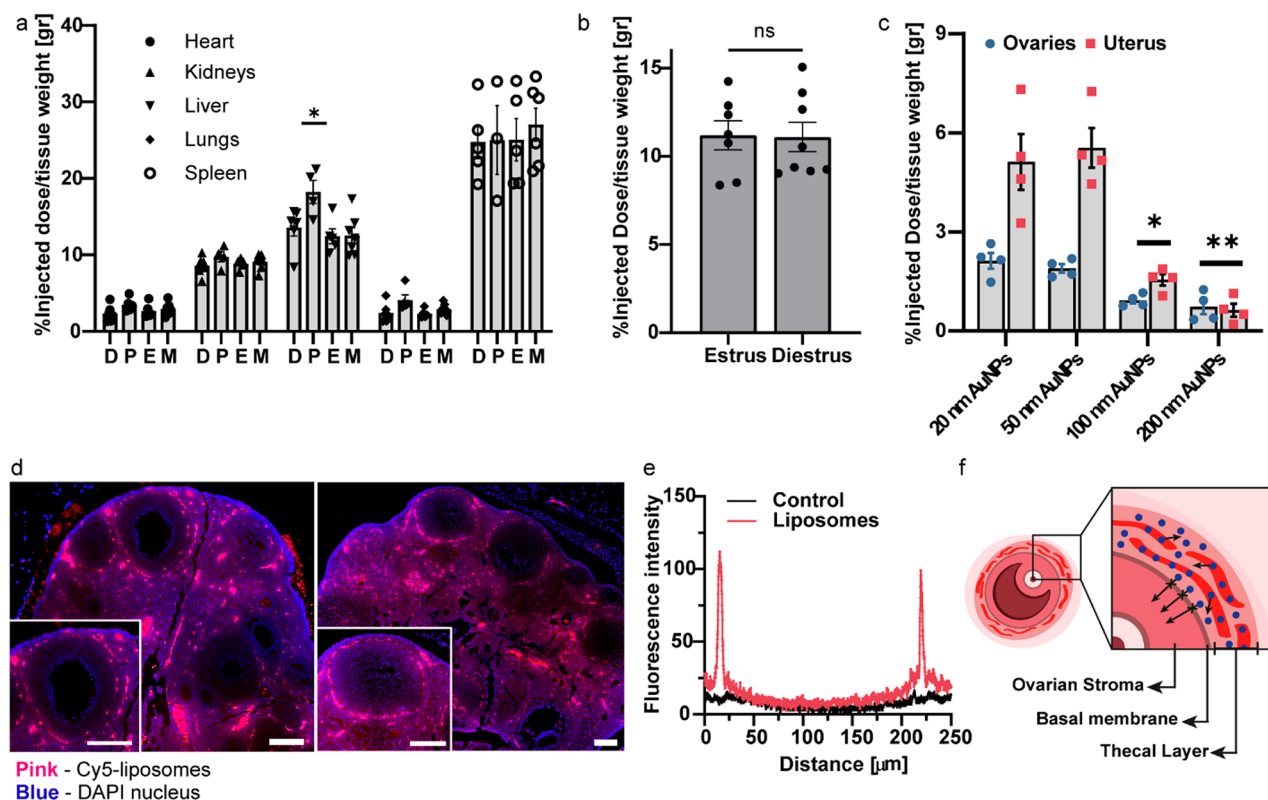


Figure 2. Size-dependence and nanoparticle biodistribution to the ovaries, uterus, and other organs. The biodistribution of Gd-lipo to the (a) heart, kidneys, liver, lung, and spleen at the different stages of the estrus cycle and (b) adrenal glands at estrus and diestrus. Size-dependent accumulation of gold nanoparticles in the ovaries (blue circles) and the uterus (red squares) 24 h after i.v. injection during the estrus stage ($n = 4$ for all groups) (c). 80 nm liposomes were detected at the blood–follicle barrier as demonstrated by fluorescent histology images of Cy5-labeled liposomes' (pink) localization in the ovary (nuclei, blue) 24 h after i.v. injection (d, scale bar 100 μm). The line profile of the fluorescent intensity signal across a single follicle shows that the liposomes surround the follicle, indicated by two peaks in the dye signal (e). Illustration of the blood–follicle barrier shows the liposomes (blue) on the basal membrane of the follicle, which are restricted to the thecal layer around the follicle (f). Results are shown as mean \pm SEM. Unpaired two-tail t test was used for statistical analysis of a. One-way ANOVA and Tukey's t test were used for statistical analysis of b and c. * $p < 0.05$, ** $p < 0.01$.

RESULTS AND DISCUSSION

The female reproductive system undergoes cyclic physiological changes timed with the monthly menstrual cycle. We studied the accumulation of nanoparticles in the uterus, ovaries, and inside the follicles before, during, and after ovulation. For this, we used gold nanoparticles of different sizes, as well as lipid nanoparticles labeled with fluorescent dyes, an MRI contrast agent (gadolinium, Gd), or ^{111}In -radio-labeled liposomes. Then, we tested the effect of doxorubicin-loaded nanoparticles on breast and ovarian cancer therapy, at different stages of the menstrual cycle. Finally, we studied the effect of doxorubicin-loaded liposomes on ovarian health and fertility in mice, considering their menstrual stage.

Maximal Nanoparticle Accumulation in the Reproductive System Was Measured during Ovulation. The menstrual cycle of the female mouse is divided into four stages: diestrus, proestrus, estrus, and metestrus. The duration of each stage varies, where the proestrus and metestrus stages usually last no longer than 24 h. The estrus stage lasts up to 48 h, while the diestrus stage is the longest stage, usually 48–72 h long but can persist also for prolonged periods of time.²⁷ The cycle stage was determined using vaginal cytology (Figure S1). To determine the biodistribution of nanoparticles toward the reproductive system, 80 nm gadolinium-loaded PEGylated liposomes (Gd-lipo, Figure 1c,d) or free-Gd were injected intravenously (i.v., Figure 1e) to the tail vein of the mice at each

of the four menstrual stages. Twenty-four hours after the injection, the cycle stage was confirmed once more, and the accumulation of either Gd-lipo (Figure 1f) or free Gd (Figure S2A) in the ovaries and the uterus (Figures 1g, S2B) was quantified using elemental analysis. Maximal accumulation of Gd-lipo was recorded during the estrus stage in the ovaries ($2.2 \pm 0.18\%$ of the injected dose per tissue weight, $n = 8$) and the uterus ($5.3 \pm 0.6\%$, of the injected dose per tissue weight, $n = 8$). The lowest accumulation occurred during the diestrus stage, where only $1.23 \pm 0.07\%$ ($n = 8$) and $2.1 \pm 0.3\%$ ($n = 7$) of the injected dose (per tissue weight) accumulated in the ovaries and the uterus, respectively. This amounts to a ~ 2 -fold ($p < 0.01$) and ~ 2.5 -fold ($p < 0.001$) increase in Gd-lipo accumulation during the estrus stage compared to the diestrus stage at the ovaries and uterus, respectively. The accumulation of Gd-lipo during the proestrus ($1.5 \pm 0.2\%$, $n = 10$ for ovaries; $3.9 \pm 0.4\%$, $n = 10$ for uterus) and the metestrus ($1.6 \pm 0.1\%$, $n = 8$ for ovaries; $3.2 \pm 0.5\%$, $n = 8$ for uterus) stages was significantly lower than during the estrus stage. In both the uterus and the ovaries, throughout the estrous cycle stages, the amount of free Gd compared to Gd-lipo was significantly lower ($p < 0.0001$, Figure S2), confirming that the quantified Gd originated from liposomal accumulation. Furthermore, we quantified that merely $14.2 \pm 8.5\%$ Gd is released from Gd-liposomes after 24 h at 37 $^{\circ}\text{C}$ (Figure S3). From here forth, we focus our comparison on two ovulation stages: diestrus and estrus.

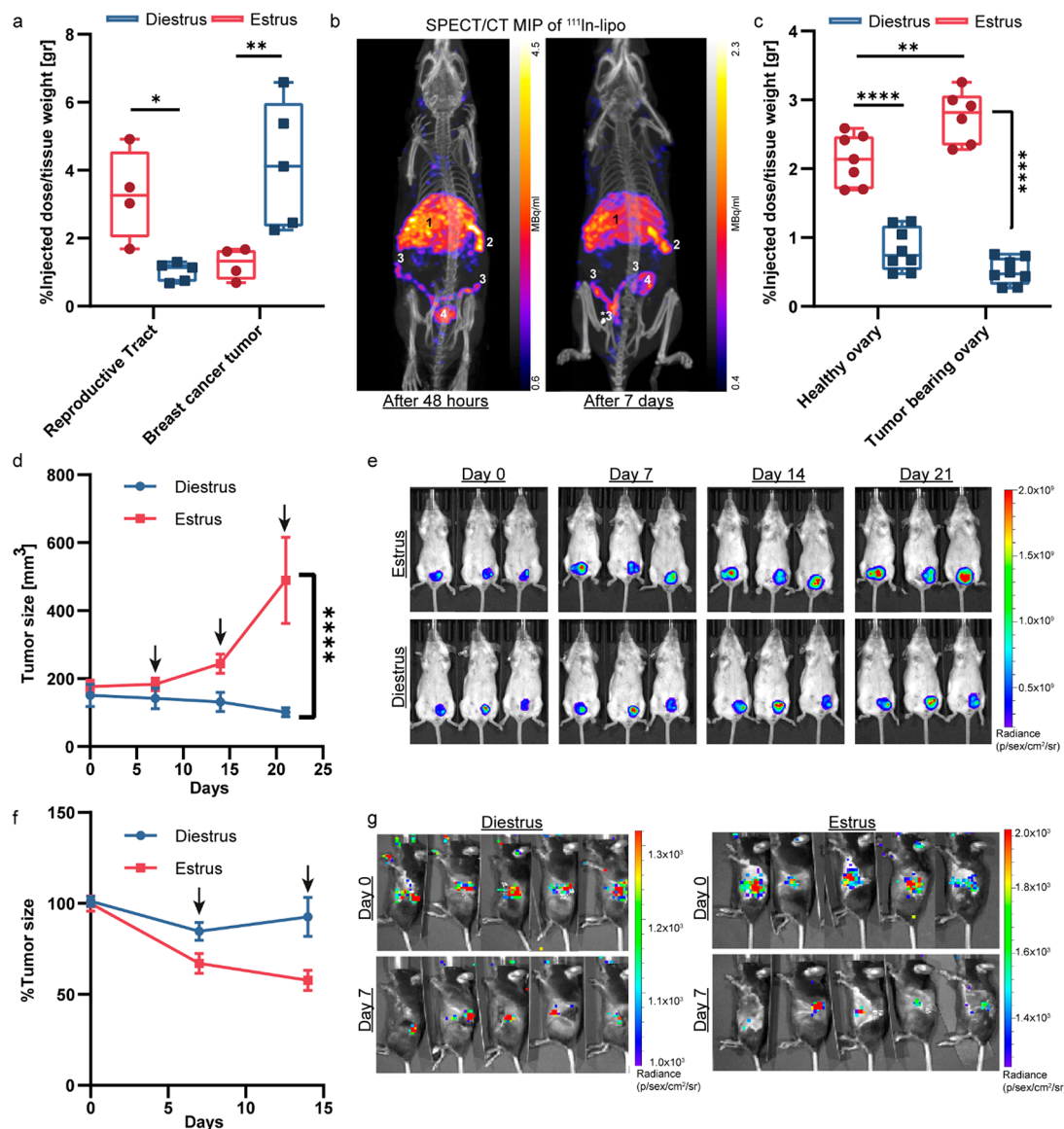


Figure 3. Biodistribution of liposomes to breast and ovarian cancer tumors and the efficacy of cancer treatment are affected by the female mouse cycle. During the estrus stage, Gd-liposomes accumulate in the reproductive system ($n = 4$) at higher levels than in orthotopic triple-negative murine (4T1) breast cancer tumors ($n = 4$). In contrast, during the diestrus stage nanoparticles shift toward the tumor ($n = 5$) and away from the reproductive system ($n = 5$) (a). Maximum intensity projection (MIP) SPECT/CT images of an MDA-MB-231 breast cancer tumor-bearing mouse after i.v. injection of ^{111}In -lipo. Accumulation is detected in the liver (1), spleen (2), ovaries (3), uterus (3*), and the tumor (4), 48 h (right image) and 7 days (left image) after injection (b). In mice bearing orthotopic ovarian cancer in one of the two ovaries, there is increased accumulation of Gd-liposomes both in the tumor-bearing ovary (estrus $n = 6$, diestrus $n = 8$) and in the healthy ovary (estrus $n = 6$, diestrus $n = 7$) during the estrus stage, compared to the diestrus stages (c). Efficacy of DOX-lipo was evaluated using caliper measurements in a 4T1 mCherry breast cancer model during estrus ($n = 7$) and diestrus ($n = 6$). Arrows indicate treatment times (d). IVIS images of 4T1 mCherry breast cancer tumor (top, treatment during estrus; bottom, treatment during diestrus) show 3 representative mice from each group (e). For ovarian cancer, treatment efficacy of DOX-lipo was evaluated using IVIS imaging, enabled by the luciferase-expressing cells, during the estrus ($n = 5$ (days 0 and 7), $n = 2$ (day 14)) and diestrus stages ($n = 5$ (days 0 and 7), $n = 3$ (day 14)). Arrows indicate treatment times (f). IVIS images of luminescent ovarian cancer tumor (left panel, treatment during diestrus; right panel, treatment during estrus) (g). Results are shown as mean \pm SEM. Two-way ANOVA and Tukey's t test were used for statistical analysis of a–c and e. ** $p < 0.01$, *** $p < 0.001$, **** $p < 0.0001$. Images a and b were created using BioRender.

To further assess the enhanced nanoparticle accumulation during estrus, we visualized the reproductive tract 24 h after an i.v. injection of 80 nm liposomes labeled with a Cy5-lipid (Figure 1h). The fluorescent intensity in the ovaries was highest during the estrus stage compared to the diestrus, proestrus, and metestrus stages (Figure 1h). These fluorescent results corroborate the quantitative Gd-lipo biodistribution findings shown above.

Increased Blood Vessel Density during the Ovulatory Stage. At the time of follicle development, in preparation for ovulation, new blood vessels are formed in the thecal layer surrounding the follicle (Figure 1a,b).²⁸ To validate the increase in blood vessel density around developing follicles during the ovulatory stages, anti-CD31 immunohistochemistry was performed (marked with a white dashed line in the image inset, Figure 1i,j), and staining intensity was quantified (Figure 1k).

The coverage of CD31-positive cells in the thecal layer is 4-fold higher during the estrus stage than in the diestrus stage (Figure 1k, $p < 0.0001$). The increased vascularity during the estrous cycle is restricted to the reproductive system, driven by VEGF secretion.¹ Higher VEGF levels also lead to capillary leakiness and increased permeability, thus enabling nanoparticle extravasation through gaps in the endothelium present during the proestrus and estrus stages.⁵

Nanoparticles Are Engulfed by the Cells of the Reproductive System. We sought to validate that the nanoparticles are taken up by the cells of the reproductive system. For this, lipid nanoparticles loaded with firefly luciferase encoding mRNA (mLuc-LNPs) were i.v. injected (250 $\mu\text{g}/\text{kg}$) to healthy female mice during the estrus stage. Twenty-four hours later, luciferase expression and bioluminescence were recorded in the ovaries and uterus using whole animal IVIS imaging, compared to untreated mice (Figure 1l). These results indicate that the LNPs penetrate into the ovarian cells where the mRNA payload is expressed by the cellular machinery.

Biodistribution of Nanoparticles to Other Organs. We studied the biodistribution of 80 nm liposomes to other organs during the different stages of the menstrual cycle. No significant difference in liposomal accumulation was recorded in the heart, lungs, kidneys, and spleen (Figure 2a) during the different stages of ovulation. However, the liver displayed a rise in liposomal accumulation during the proestrus stage compared to the diestrus, estrus, or metestrus stages ($p < 0.05$). This increase may be related to elevated estrogen levels during proestrus and its effect on cytochrome P450 liver metabolism.²⁹ While we and others observed nanoparticle accumulation in the adrenal glands postintravenous administration,^{6,30} we did not observe a differences in the accumulation of 80 nm Gd-lipo between the estrus and diestrus stages (Figure 2b).

Nanoparticle Accumulation in the Reproductive System Is Size-Dependent. To test whether the ovaries have a size cutoff, PEGylated gold nanoparticles (AuNPs) of different sizes (20, 50, 100, and 200 nm) were injected intravenously during the estrus stage.³¹ We chose to conduct the size cutoff studies using AuNPs, due to their distinct size accuracy. Accumulation of AuNPs in the ovaries and the uterus was quantified 24 h postinjection using elemental analysis (Figure 2c). After 24 h, $2.1 \pm 0.2\%$ of the injected dose normalized to the tissue weight was detected in the ovaries for 20 nm AuNPs and $1.9 \pm 0.1\%$ for 50 nm AuNPs was detected in the ovaries. Contrarily, only $0.9 \pm 0.1\%$ or $0.7 \pm 0.2\%$ of the 100 and 200 nm AuNPs, respectively, reached the ovaries (Figure 2c). In a similar pattern, 20 and 50 nm AuNPs accumulated at higher doses in the uterus compared to 100 and 200 nm particles (Figure 2c). Based on these results, 100 nm AuNPs accumulated ~ 2 -fold less in the ovaries ($p < 0.05$) and ~ 3.5 -fold less in the uterus ($p < 0.05$) compared to smaller AuNP sizes, while 200 nm AuNPs accumulated ~ 2.5 -fold less in the ovaries ($p < 0.01$) and ~ 8 -fold less in the uterus ($p < 0.01$) compared to AuNPs of smaller sizes. Nanoparticle biodistribution is influenced by various factors such as chemical composition, size, and charge as well as the adsorption of a protein corona to the nanoparticle surface.³² Having said this, we and others report that ovarian accumulation occurred using different types and sizes of polymeric nanoparticles.^{6,30}

Liposomes of 80 nm Are Restricted outside the Blood–Follicle Barrier. The blood–follicle barrier (BFB) forms during the early follicle stage and remains as a protective biological barrier until ovulation, at which point the barrier

ruptures to release the oocyte.³³ Changes in the BFB structure throughout the follicular development allow strict regulation of the intrafollicular fluid composition. The BFB protects the developing oocyte from toxic and foreign molecules while supplying it with necessary nutrients and growth factors.³⁴ Twenty-four hours post i.v. injection, 80 nm liposomes were found surrounding the follicle, specifically at the outer thecal layer (Figure 2d). Fluorescence intensity measurements across a single follicle demonstrated that the liposomal signal is restricted outside the follicle, signified by two distinct peaks, with baseline signal recorded inside the follicle itself (Figure 2e), suggesting that 80 nm liposomes do not cross the BFB in an efficient manner (Figure 2f).

The Estrous Cycle Affects Tumor Biodistribution and Nanomedicine Efficacy. Nanomedicines are used as *first-line* treatments of several types of cancer, including ovarian and breast cancer.^{35,36} We tested the effect of the ovulatory cycle on nanoparticle accumulation in tumors. For this, we measured the biodistribution of 80 nm liposomes during estrus and diestrus stages in mice bearing orthotopic triple-negative breast cancer (4T1) tumors or epithelial ovarian cancer. Gd-lipo, 80 nm in diameter, were i.v. injected to tumor-bearing mice, and their accumulation was quantified 24 h postadministration. In the breast cancer model, 3.3-fold more liposomes accumulated in the tumor during the diestrus stage compared to the estrus stage (Figure 3a, $p < 0.01$). Interestingly, the opposite trend was observed in the reproductive system, where 3.2-fold more liposomes accumulated during the estrus stage than the diestrus stage (Figure 3a, $p < 0.05$). Thereby, the highest liposomal accumulation in the tumor was recorded during the diestrus stage, and on the contrary, the highest accumulation in the reproductive system was during the estrus stage. These findings suggest that during the estrus stage the accumulation of nanoparticles is shifted toward the reproductive system rather than the tumor (Figure 3a). To further visualize nanoparticle accumulation in the reproductive system, mice bearing human breast cancer tumors (MDA-MB-231) were i.v. injected with 100 nm ¹¹¹In-labeled PEGylated liposomes (¹¹¹In-lipo) and scanned by SPECT/CT 48 h and 7 days postinjection (Figure 3b).³⁷ High levels of ¹¹¹In were detected in the reproductive system, liver, spleen, and the tumor itself, in comparable intensities, even 7 days after injection, demonstrating accumulation of nanoparticles in the reproductive system in the presence of a tumor.

Next, we tested our research hypothesis using an ovarian cancer model. A tumor was induced only in one of the two ovaries in each mouse, to compare liposomal accumulation between the healthy ovary and the tumor-bearing ovary. In the healthy ovary, 2.6-fold more liposomes accumulated during estrus compared to the diestrus stage (Figure 3c, $p < 0.0001$), similarly to the accumulation in healthy mice (Figure 1f). Notably, 5.4-fold more liposomes reached the tumor-bearing ovary during estrus, compared to diestrus (Figure 3c, $p < 0.0001$). This increased uptake toward the tumor-bearing ovary implies an additional effect of tumor vascularization.³⁸ In the diestrus stage, slightly higher accumulation was observed in the healthy ovary compared to the tumor-bearing ovary; this result was statistically insignificant.

We then tested the efficacy of DOX-lipo effect on breast and ovarian cancer models, treating during either the estrus or diestrus stages. Mice bearing orthotopic triple-negative breast cancer tumors were treated weekly with an intravenous administration of DOX-lipo, during either the estrus stage or

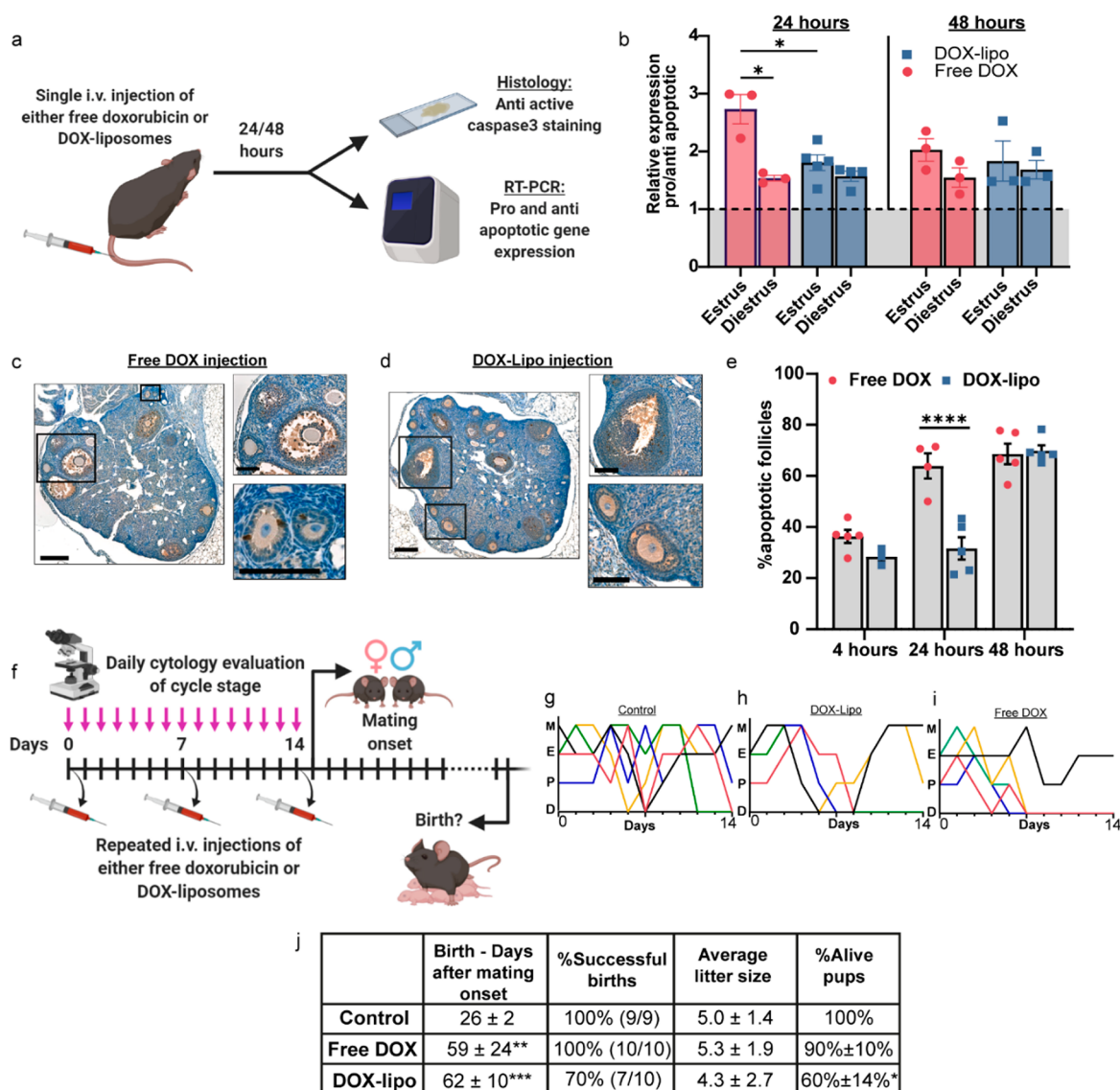


Figure 4. Doxorubicin-loaded liposomes delayed ovarian toxicity and affected fertility in female mice. Healthy female mice received an i.v. injection of either free DOX or DOX-lipo, and the ovaries were analyzed by immunohistochemistry and RT-PCR 24 and 48 h post drug administration (a). RT-PCR of pro-/antiapoptotic gene expression (Bcl2 and BAX) during estrus (24 h, $n = 3$ for free DOX, $n = 5$ for DOX-lipo, 48 h, $n = 3$ for both groups) and diestrus (24 h, $n = 3$ for free DOX, $n = 4$ for DOX-lipo, 48 h, $n = 3$ for both groups) are shown as the relative expression of the ratio between pro- (BAX) and antiapoptotic (bcl2) genes (b). Immunohistochemistry of anti-active caspase 3 24 h after i.v. injection during the estrus stage of either free DOX (c) or DOX-lipo (d) shows apoptotic follicles (brown signal) with higher signal in the follicles in the free-DOX group. Quantification of the total signal output from the follicles demonstrated that more follicles were apoptotic in the free-DOX group ($n = 4$) compared to DOX-lipo ($n = 5$) 24 h after i.v. injection; however apoptosis levels become comparable after 48 h ($n = 5$ for both groups) (e). Healthy female mice received repeated i.v. injections of either free DOX ($n = 10$) or DOX-lipo ($n = 10$) once a week for 3 consecutive treatments, and their cycle stage was recorded daily to be compared to that of the control group ($n = 9$) that was not injected (f). The estrous cycle in each group is demonstrated in graphs g–i, where each line represents a single mouse. Compared to the control group (g), mice in the DOX-lipo (h) and the free-DOX (i) groups had a disrupted cycle. After the third injection, females were housed with males, and the day of birth, litter size, and pups' viability were recorded (j). The time until pregnancy was significantly longer for both the free-DOX and the DOX-lipo group; however the pups' viability was lower for the DOX-lipo group. Results are shown as mean \pm SEM. Three-way ANOVA and Tukey's t test (b), two-way ANOVA and Tukey's t test (e and % alive pups in j), and Dunnett's T3 t test (days until birth in j) were used for statistical analysis. * $p < 0.05$, ** $p < 0.01$, *** $p < 0.001$, **** $p < 0.0001$. Images a and f were created using BioRender.

diestrus stage, for three treatment cycles (Figure 3d,e). Before each treatment, estrus was induced by exposing the female mice to bedding taken from cages that housed male mice. The mice in the diestrus group showed a persistent diestrus stage resulting from housing in a cage with 5 females. Furthermore, prior to the treatment, the cycle stage was determined and mice that did not meet the stage criteria were excluded. After 21 days, the average tumor size in the estrus group increased by $276 \pm 58\%$ compared

to day 1, while in the diestrus treated group the tumor reduced to $72 \pm 6\%$ of the initial size ($p < 0.0001$, Figure 3d). This result correlates with the biodistribution profile during the estrus stage, in which the nanoparticles accumulated preferentially at the reproductive system rather than at the tumor, resulting in decreased therapeutic efficacy. Contrarily, treating breast cancer tumors during the diestrus stage resulted in tumor reduction,

indicating improved therapeutic efficacy compared to treatment during the estrus stage.

When the reproductive system is the target of the nanomedicine treatment, as in ovarian cancer, the therapeutic outcome is favorable. For example, treating ovarian cancer with DOX-lipo was superior during the estrus stage compared to the diestrus stage (Figure 3f,g). After 14 days, the average tumor size of the diestrus group was ~1.6-fold larger than the average tumor volume of the estrus group, as more liposomes reached the tumor-bearing ovary during ovulation, thus increasing efficacy.

Doxorubicin-Loaded Liposomes Delayed Ovarian Toxicity. We evaluated the effect of liposomal doxorubicin versus free doxorubicin on ovarian toxicity.¹⁴ Healthy female mice received an i.v. injection of either free doxorubicin (free-DOX) or doxorubicin-loaded liposomes (DOX-lipo) during the estrus and diestrus stages (Figure 4a). After 24 or 48 h, the ovaries were collected and RT-PCR analysis of pro- and antiapoptotic genes (Bcl2 and BAX) was performed. Ovarian toxicity was recorded in all the experimental groups compared to the nontreated control (Figure 4b). The highest apoptosis level was measured 24 h after free-DOX injection during estrus ($R = 2.7 \pm 0.2$, $n = 3$, ratio between pro- and antiapoptotic gene expression normalized to healthy mice) and was significantly higher ($p < 0.05$) compared to injection during the diestrus stage ($R = 1.5 \pm 0.08$, $n = 2$). Furthermore, apoptosis levels 24 h after injection at the estrus stage were ~1.5-fold higher for the free-DOX group than the DOX-lipo group ($p < 0.05$). Interestingly, after 48 h the apoptosis levels in both groups were comparable and no significant differences between the liposomal versus free drug groups were observed. Immunohistochemistry analysis confirmed that the apoptotic effect took place inside the follicles (Figure 4c,d). Antiactive caspase3 staining was used to detect apoptotic follicles 4, 24, and 48 h after injection of either free DOX or DOX-lipo during the estrus stage.

At all time points, the larger the follicle, the greater the apoptosis levels were (Figure S4). This may be explained by an increased blood supply to larger follicles³⁹ and resulting increased drug exposure. After 24 h, free-DOX-treated mice had significant apoptosis in both small and large follicles (Figure 4c) compared to the DOX-lipo group, which showed no apoptotic signs in the smaller follicles (Figure 4d). The overall percentage of apoptotic follicles (Figure 4e) after 4 h was slightly higher for the free-DOX-treated ovaries ($36 \pm 5.6\%$, $n = 5$) compared to the DOX-lipo group ($28 \pm 3.3\%$, $n = 3$). After 24 h, the percentage of overall apoptotic follicles increased significantly ($p < 0.0001$) for the free-DOX-treated group ($64 \pm 10\%$, $n = 4$) compared to the DOX-lipo group, which remained constant ($32 \pm 10\%$, $n = 5$). Surprisingly, after 48 h, there was no significant increase in apoptosis in the free-DOX group ($69 \pm 9\%$, $n = 5$), while the percentage of apoptotic follicles spiked significantly ($p < 0.0001$) in the ovaries of DOX-lipo-treated mice ($70 \pm 5\%$, $n = 5$), which correlates with the RT-PCR data (Figure 4b). Free-DOX was previously shown to cross the BFB and damage the developing oocytes.^{14,40} These results suggest the delayed effect of the DOX-lipo is due to initial liposomal accumulation in the ovaries, followed by drug release that induces the toxicity.

Treatment with Doxorubicin-Loaded Liposomes Affected Fertility. We further explored the effect of nanoparticulate doxorubicin on fertility. Healthy female mice were divided into three groups: free-DOX treated, DOX-lipo treated, and nontreated control. The two treatment groups received

three rounds of weekly i.v. injections, and their cycle stage was monitored daily (Figure 4f). After three treatments, the female mice were housed with male mice for mating. The day of birth was monitored in addition to the litter size, pups' weights, and viability after birth. The effect of both DOX and DOX-lipo was apparent during the treatments, as the estrous cycle was disrupted in the DOX-lipo-treated group and the free-DOX-treated group (Figure 4g–i), compared to the control group, where the estrous cycle remained normal. All mice (100%) in the control group had successful births 26 ± 2 ($n = 9$) days after mating onset (Figure 4j). In contrast, time until first litter was 59 ± 24 days ($n = 10$) for the free-DOX-treated group and 62 ± 10 days ($n = 10$) in DOX-lipo group.

Furthermore, while all mice in the free-DOX group were pregnant and gave birth (100% births), only 70% of the mice in the DOX-lipo group conceived. This implies that the mice in the free DOX group regained their ability to ovulate. The average litter size was 5 ± 1.4 , 5.3 ± 1.9 , and 4.3 ± 2.7 pups for the control, free-DOX, and DOX-lipo group, respectively. The viability of the pups was 100% and $90 \pm 10\%$ for the control and the free-DOX groups, respectively, while it declined to $60 \pm 14\%$ for the DOX-lipo group ($p < 0.05$). These results suggest that the treatment with DOX-lipo affects ovarian viability. This can be explained by the long retention time of the liposomes in the ovaries compared to free molecule drugs that are cleared rapidly.⁴¹

CONCLUSIONS

Our study demonstrates that the menstrual cycle affects the biodistribution of nanoparticles toward the female reproductive system, affecting nanomedicine activity. Biological sex, as an important factor in preclinical research and clinical trials, is already encouraged by the regulatory bodies;⁴² however in the field of nanotechnology these considerations are still under-researched. While in many cases female cancer patients undergo ovulation suppression as part of the therapeutic protocol, not all patients undergo this process.^{43–45} We therefore propose that the menstrual cycle should be accounted for when devising nanomedicine-based cancer treatments to females.

While enhanced accumulation in the reproductive system may affect fertility, this biodistribution pattern can also be leveraged as a treatment strategy to improve the treatment of various malignancies and conditions.

We conclude that the state of the menstrual cycle should be taken into consideration in designing and implementing therapeutic nanotechnologies.

MATERIALS AND METHODS

Estrous Cycle and Cytology. Healthy 8–10-week-old C57BL/6 female mice were housed 5 per cage in standard laboratory conditions and were exposed to 12 h of light and 12 h of dark. All animal experiments were approved by, and in compliance with, the institutional and ethical committee at the Technion (ethics number IL0730517). The animals' well-being was monitored regularly. Ovulation and cycle synchronization was achieved by mixing solid bedding from the cages of male mice with the bedding of the female mice cage for 2 days.⁴⁶ The estrous cycle stage of each female mouse was determined using the cytology method, which was performed daily at the same time (7AM–9AM). Vaginal cytology is a common method for cycle stage evaluation by simply observing the different cell populations in stained vaginal smears taken from the vaginal opening of the mouse.⁴⁷ To collect a vaginal smear, 10 μ L of sterile water was carefully pipetted on the vaginal opening and then placed on a glass slide to air-dry. The dry smears were stained using Jorvet Dip Quick

staining kit (Jorgensen Laboratories) and examined under a light microscope. The cycle stage was determined by observing the cell population (Figure S1). Before experiment initiation, two consecutive estrous cycles were confirmed for each mouse.

Gadolinium-Loaded Liposome Preparation. Gd liposomes were prepared as described before.⁴⁸ Briefly, a lipid mixture of hydrogenated soybean phosphatidylcholine (HSPC; Avanti Polar Lipids, Alabaster, AL, USA), cholesterol (Sigma-Aldrich, Rehovot, Israel), and 1,2-distearoyl-*sn*-glycero-3-phosphoethanolamine-*N*-methoxypolyethylene glycol 2000 (DSPE-PEG2000; Avanti Polar Lipids, Alabaster, AL, USA), in molar percentages of 56:39:5, was dissolved in pure ethanol at 70 °C. The lipid mixture was injected into a Dulbecco's phosphate buffer saline (PBS; Sigma-Aldrich, St. Louis, MO, USA) solution containing 167 mg/mL of Gd-DTPA diethylenetriamine-pentaacetic acid gadolinium(III) dihydrogen salt hydrate (Gd; Sigma-Aldrich, Rehovot, Israel) to obtain a final lipid concentration of 50 mM. The liposomes were downsized to 80 nm using a Lipex extruder (Northern Lipids, Vancouver, Canada) at 65 °C through 400, 200, 100, 80, and 50 nm Nuclepore polycarbonate membranes (Whatman, Newton, MA, USA). Free Gd-DTPA was removed using dialysis in a 12–14 kDa membrane (Spectrum Laboratories, Inc., USA) against PBS (1:1000 volume ratio) at 4 °C and exchanged three times. Average liposome size was measured using a Zetasizer Nano ZSP (Malvern Instruments, UK) in disposable polystyrene cuvettes after liposomes were diluted 1:100 in PBS, and cryo-TEM was performed as described previously.⁴⁸

Cy5-Labeled Liposome Preparation. Cy5-labeled liposomes were prepared in the same method as Gd-liposomes only without Gd added to the PBS solution. A 1% molar percentage of DSPE-Cy5 was added to the lipid mixture before injection to the PBS solution.

mRNA-LNP Preparation. LNPs of 60 nm were synthesized by a microfluidic mixing device, Nanoassemblr (Precision Nanosystems, Vancouver BC), as mentioned before.⁴⁹ Briefly, one volume of lipid mixture of ionizable lipid 14,⁴⁹ DSPC, cholesterol, and DMG-PEG at 40:10.5:47.5:2 mol ratio in ethanol and three volumes of mRNA (1:20 w/w mRNA to cationic lipid) in acetate buffer were mixed through a microfluidic mixer at a combined flow rate of 12 mL/min. The resultant mLuc-LNPs were dialyzed against PBS (pH 7.4) for 16 h to remove ethanol. The size and uniformity of LNPs were analyzed by dynamic light scattering (Malvern Instruments Ltd., Worcestershire, UK).

Doxorubicin-Loaded Liposome Preparation. Doxorubicin (TEVA Israel) was actively loaded into a 80 nm liposome using the ammonium sulfate gradient method.⁵⁰ A lipid mixture of HSPC, cholesterol, and DSPE-PEG2000 in molar percentages of 56:39:5, respectively, was dissolved in pure ethanol at 70 °C. The dissolved lipids were injected into 120 mM ammonium sulfate solution to reach a final concentration of 50 mM total lipids. The liposomes were downsized to 80 nm using an extruder at 70 °C. Dialysis was performed in 12–14 kDa dialysis membrane against 10% w/w sucrose and 10 mM histidine at pH 6.5 (1:1000 volume ratio) and exchanged three times. For active loading, DOX was dissolved in 10% w/w sucrose and added to the ammonium sulfate liposomes to reach a final concentration of 2 mg/mL. The mixture was placed at 70 °C at 600 rpm for 1 h. The DOX-loaded liposomes were dialyzed in 12–14 kDa dialysis membrane against 10% w/w sucrose and 10 mM histidine pH 6.5 (1:1000 volume ratio) for 24 h.

Gd-Liposome Biodistribution. After determining the estrous cycle, 200 μ L of Gd-liposomes was injected i.v. into the tail vein of healthy female mice. Twenty-four hours after injection, the mice were sacrificed and the ovaries, uterus, kidneys, spleen, liver, heart, and lungs were collected and weighed. The organs were disintegrated to ash at 550 °C for 5 h. The ashes were dissolved in 5 mL of 1% nitric acid, and the mixture was filtered through 0.45 μ m syringe filters and taken for ICP-OES analysis.

Gold Nanoparticle Biodistribution. PEGylated gold nanoparticles (20, 50, and 100 nm) were purchased from NanoCompasix (San Diego, CA, USA), and 200 nm PEGylated gold nanoparticles were purchased from NanoPartz (Loveland, CO, USA). After determining the estrous cycle, 100 μ L of 1 mg/mL gold nanoparticles was injected i.v. into the tail vein of healthy female mice. Twenty-four hours after

injection the mice were sacrificed and the ovaries and uterus were collected and weighed. The organs were dissolved overnight in aqua-regia solution and then heated at 60 °C for 1 h. The dissolved organs were resuspended in double-distilled water to reach an acid concentration of 1%. The mixture was filtered through 0.45 μ m syringe filters and taken for inductively coupled plasma–optical emission spectroscopy (ICP-OES) analysis.

Elemental Analysis of Gd and Au. Gadolinium and gold samples were analyzed using a S110 ICP-OES (Agilent, CA, USA). Calibration curves for each element were obtained from a calibration standard (Sigma-Aldrich, Rehovot, Israel) diluted in 1% nitric acid. Gd emission was measured at 335.048 and 342.246 nm. Au emission was measured at 242.794 and 267.594 nm. The concentration at each wavelength was calculated by the ICP-OES software according to the obtained calibration curve. The measurements from both wavelengths were averaged for each element. The obtained concentration was divided by the injected dose concentration to obtain the percentage out of the injected dose and then divided by the organ's weight for normalization.

Ex Vivo IVIS Imaging. A 200 μ L amount of Cy5-labeled liposomes was injected i.v. into the tail vein of healthy female mice after determining the estrous cycle stage. Twenty-four hours after injection the mice were sacrificed and the reproductive system was imaged *ex vivo* using the IVIS SpectrumCT pre-clinical *in vivo* imaging system (PerkinElmer, MA, USA) at an excitation of 570 nm and emission of 620 nm, binning 8, *f*-stop 2 and 3 s exposure. A control (not-injected) mouse was used for analysis. All images were analyzed using the LivingImage software.

Fluorescent Histology Analysis. A 200 μ L amount of Cy5-labeled liposomes was injected i.v. into the tail vein of healthy female mice after the estrous cycle stage was determined. Twenty-four hours after injection the mice were sacrificed, and the reproductive system was fixed using formalin solution neutral buffered 10% histological tissue fixative (Sigma-Aldrich, Rehovot, Israel) at 4 °C for at least 24 h before embedding in paraffin and sectioning (3–5 μ m sections). Slides were deparaffinized in a xylene/ethanol gradient as follows: soaked in xylene for 3 min, xylene/ethanol (1:1 vol ratio) for 3 min, absolute ethanol for 3 min, 95% ethanol for 3 min, 70% ethanol for 3 min, and 50% ethanol for 3 min, and finally placed in tap water. Nuclei blue fluorescent staining was done using Invitrogen Molecular Probes NucBlue Fixed Cell ReadyProbes reagent (Fisher Scientific, Waltham, MA, USA) incubated for 5 min followed by rinsing with tap water. The slides were imaged with a Leica DMI8 inverted fluorescent microscope (Leica Microsystems GmbH, Wetzlar, Germany) using 40 \times magnification with exposure times of 400 ms for the DAPI channel and 900 ms for the Cy5 channel.

Immunohistochemistry Analysis. Tissue was collected and fixed for 24 h at 4 °C in formalin solution neutral buffered 10% histological tissue fixative (Sigma-Aldrich, Rehovot, Israel). Fixed tissue was embedded in paraffin and sectioned to 10 μ m sections. Slides were deparaffinized in a xylene/ethanol gradient as follows: soaked in xylene for 3 min, xylene/ethanol (1:1 vol ratio) for 3 min, absolute ethanol for 3 min, 95% ethanol for 3 min, 70% ethanol for 3 min, and 50% ethanol for 3 min, and finally placed in tap water. Antigen retrieval was done in 10 mM trisodium citrate solution at pH 6 titrated with HCl. A 2.5% ready-to-use normal goat serum (Vector Laboratories) was used for blocking. Incubation with primary antibody was done at 4 °C overnight with either anti-CD31 diluted 1:100 (ab28364, Abcam, Cambridge, MA, USA) or anti-active caspase3 diluted 1:100 (ab2302, Abcam). For blocking of endogenous peroxidase activity, the slides were incubated for 30 min in 0.3% hydrogen peroxide solution and then washed in tap water before incubation with ready-to-use secondary goat anti-rabbit antibody conjugated to HRP (MP7451 kit, Vector Laboratories) for 40 min at room temperature. For color development, slides were incubated with DAB solution (SK4105 kit, Vector Laboratories) for 3 min, washed with tap water, and counterstained with hematoxylin. Slides were scanned using 3DHitech Panoramic 250 Flash III automated slide scanner (3DHitech, Budapest, Hungary) at 40 \times magnification. For the CD31-positive slides, the stained area around follicles was quantified using Fiji analysis software. Threshold was selected based on the same tissue slide stained with only the secondary-HRP antibody.

Apoptosis Experiment. Healthy female mice were divided into 3 groups: control, DOX-liposomes, and free DOX. After determining the estrous cycle stage, mice were injected with 100 μL of 5 mg/kg of either DOX-liposomes or free DOX. The mice were sacrificed after either 24 or 48 h, and the reproductive system was taken for either mRNA extraction for RT-PCR or fixation in 10% formalin solution neutral buffered histological tissue fixative for immunohistochemistry analysis.

RT-PCR Analysis. mRNA was extracted from ovaries using a NucleoSpin RNA kit (#740955.50, Macherey-Nagel, Germany) according to the manufacturer's protocol. mRNA was quantified by measuring absorbance at 260 nm with a NanoQuant plate in an Infinite 200PRO plate reader (TECAN, Männedorf, Switzerland). A 400 ng amount of mRNA was used for cDNA synthesis in a 20 μL reaction volume using a high-quality cDNA synthesis kit (PCR Biosystems, Wayne, PA, USA). Real-time PCR was performed on a qRT-PCR CFX Bio-Rad machine (Bio-Rad laboratories, Hercules, CA, USA) using qPCR BIO Fast qPCR SyGreen Blue Mix Hi-ROX (PCR Biosystems). The GAPDH gene was used as a housekeeping gene for normalization. Primer sequences:

- Bcl2: Forward-ATGCCTTTGTGGAACATATATGGC; Reverse-GGTATGCACCCAGAGTGATGC,
- BAX: Forward-TGAAGACAGGGCCCTTTTGT; Reverse-AATTCGCCGGAGACACTCG,
- GAPDH: Forward-TGCACCACCAACTGTCTAG; Reverse-GGATGCAGGGATGATGTTT

Mating Experiment. Healthy, 8–10-week-old C57BL/6 female mice were divided into 3 groups: control, free DOX, and DOX-liposomes. The estrous cycle of all the mice was monitored daily. A 5 mg/kg concentration of either free DOX or DOX-liposomes was injected i.v. into the mouse tail vein every 7 days for a total of three injections per group (day 0, 7, and 14). After the third injection, two females were placed with a healthy C57BL/6 male and were allowed to mate. Pregnancy was monitored, and the day of birth, number, viability, and weight of pups were documented.

Cell Culture. MOSE cells were kindly provided by Novocure Ltd. Triple-negative breast cancer 4T1 mCherry cells were purchased from ATCC. Cells were mycoplasma free. MOSE-luc cells were cultured in Dulbecco's modified Eagle medium Nutrient Mixture F-12 (DMEM-F12, Biological Industries, Israel) supplemented with 10% fetal bovine serum (FBS), 100 IU/mL penicillin, 100 $\mu\text{g}/\text{mL}$ streptomycin, and 2 mM L-glutamine (Biological Industries) and grown at 37 $^{\circ}\text{C}$; 5% CO_2 . 4T1 mCherry cells were cultured in Roswell Park Memorial Institute medium (RPMI; Sigma-Aldrich, Rehovot, Israel) supplemented with 10% FBS, 100 IU/mL penicillin, 100 $\mu\text{g}/\text{mL}$ streptomycin, and 2 mM L-glutamine and grown at 37 $^{\circ}\text{C}$; 5% CO_2 . To detach the cells, they were first incubated in fresh medium for 1 h, washed with PBS, and incubated with trypsin for 5 min. The cells were collected by centrifugation at 200g for 5 min. The cell pellet was suspended in fresh medium, and cell concentration was measured using a cell counter.

Breast Cancer Model. A 50 μL amount of 250 000 4T1 mCherry cells was suspended in PBS and injected subcutaneously directly into the mammary fat pad of healthy 8–10-week-old BALB/c female mice.⁵¹ Tumor development was monitored using caliper measurements and IVIS *in vivo* fluorescent imaging. Treatment was initiated when the tumor size mean in all groups was 150 mm^3 . The mice were treated during either estrus or diestrus stages with 6 mg/kg of DOX-liposomes once a week for 21 days.

Orthotopic Ovarian Cancer Model. Healthy 8–10-week-old C57BL/6 female mice were anesthetized using a mixture of 90 mg/kg ketamine and 10 mg/kg xylazine and received 0.3 mg/kg buprenorphine for pain relief. Small incisions in the skin and peritoneum were made in the back of the animal above the ovarian fat pad. The ovary was pulled out and held in place with a bulldog clip by the ovarian fat pad. Using a 30-gauge Hamilton syringe 10 μL of 100 000 MOSE (expressing luciferase) cells suspended in equal parts of PBS and Matrigel was injected directly into the ovarian bursa. The ovary was placed gently back inside, and the peritoneum was sutured using 7–0 absorbable stitches. The skin was closed using surgical clips. The animals were placed in a 37 $^{\circ}\text{C}$ incubator until fully awake. Tumor

development was monitored using D-luciferin injection (150 mg/kg) followed by IVIS *in vivo* luminescence imaging. Treatment was initiated 2 weeks after the injection of the cells and when luminescence signal could be detected using IVIS imaging. The mice were treated during either estrus or diestrus stages with 6 mg/kg DOX-liposomes once a week for 14 days.

In Vivo IVIS Imaging. Whole animal imaging was performed in the IVIS Spectrum CT preclinical *in vivo* imaging system (PerkinElmer, MA, USA). For all imaging, the animals were placed under isoflurane anesthesia. 4T1 mCherry tumors were imaged using a fluorescent mCherry filter with the following settings: ex. 570 nm, em. 620 nm, binning 4, f-stop 2, and exposure time 3 s. Ovarian luciferase-expressing tumors were imaged using the luminescence setting with the following settings: open emission filter, binning 16, f-stop 1, and exposure time of 180 s, 12 min after i.p. injection of 150 mg/kg D-luciferin. All images were analyzed using the LivingImage software.

¹¹¹In-Liposome Radiolabeling. For the SPECT studies, PEGylated liposomal alendronate (PLA) was kindly provided by the laboratory of Prof. Alberto Gabizon (Nano-oncology Ctr., Shaare Zedek Hospital, Jerusalem, Israel). For details on the preparation see Shmeeda, *et al.*, *Journal of Drug Targeting*, 2016.⁵² Radiolabeling was performed as follows: a solution of ¹¹¹In in 0.1 M HCl (Curium, UK; approximately 110 MBq) was buffered by adding 200 μL of 0.1 M sodium acetate buffer (pH 5.5). A 10 μL oxine solution (8-hydroxyquinoline, 10 mg/mL in absolute ethanol) was added, and the mixture was heated at 50 $^{\circ}\text{C}$ for 15 min. Then 450 μL of chloroform was added, the bilayer mixture was vortexed for 5 min, and the organic phase was extracted and dried at 50 $^{\circ}\text{C}$ under a nitrogen stream. The resulting [¹¹¹In]In-oxine was redissolved in 20 μL of absolute ethanol and diluted with 50 μL of sterile saline solution.

[¹¹¹In]In-oxine (100 MBq) in ethanol/saline was added to a suspension of PLA and incubated for 30 min at 50 $^{\circ}\text{C}$. After cooling to room temperature, empty 100 nm PEGylated liposomes were added to achieve a total dose of 4 μmol of lipids per mouse. To remove unincorporated ¹¹¹In, the suspension was loaded onto a PD Minitrap G-25 size-exclusion column (Cytiva, UK) and eluted with sterile saline. The fractions containing liposomes including ¹¹¹In-PLA were collected, combined, and used for *in vivo* experiments without further modification.³⁷

Tumor Model and SPECT Imaging. On day 0, MDA-MB-231 cells expressing human sodium iodide symporter (hNIS)⁵³ were implanted in the mammary fat pad of female SCID/beige mice (6–8 weeks, Charles River, UK), between the fourth and fifth nipple. On day 14, [¹¹¹In]In-PLA (6–8 MBq ¹¹¹In, 5 mg/kg alendronate, and 4 μmol of lipids/mouse) were injected *via* the tail vein. On day 16 and day 21, the mice were scanned in a NanoSPECT/CT scanner (Mediso, Hungary; 1 mm collimators, 30 min scan). Data sets were reconstructed using a Monte Carlo-based full-3D iterative algorithm (Tera-Tomo, Mediso). Images were co-registered and analyzed using VivoQuant v2.50 (Invicro).

Statistical Analysis. For all statistical analyses, Student's *t* test (two-sided), two-way ANOVA, and three-way ANOVA were performed using Prism GraphPad software.

ASSOCIATED CONTENT

Supporting Information

The Supporting Information is available free of charge at <https://pubs.acs.org/doi/10.1021/acsnano.1c07237>.

Figures S1–S7 with additional experimental results (PDF)

AUTHOR INFORMATION

Corresponding Authors

Avi Schroeder — Laboratory for Targeted Drug Delivery and Personalized Medicine Technologies, Department of Chemical Engineering, Technion—Israel Institute of Technology, Haifa

32000, Israel; orcid.org/0000-0003-2571-5937;
Email: avids@technion.ac.il

Assaf Zinger – Laboratory for Bioinspired Nano Engineering and Translational Therapeutics, Department of Chemical Engineering, Technion–Israel Institute of Technology, Haifa 3200003, Israel; Cardiovascular Sciences and Neurosurgery Departments, Houston Methodist Academic Institute, Houston, Texas 77030, United States; orcid.org/0000-0001-7894-486X; Email: assafzinger@technion.ac.il

Authors

Maria Poley – Laboratory for Targeted Drug Delivery and Personalized Medicine Technologies, Department of Chemical Engineering, Technion–Israel Institute of Technology, Haifa 32000, Israel; orcid.org/0000-0002-5352-5690

Patricia Mora-Raimundo – Laboratory for Targeted Drug Delivery and Personalized Medicine Technologies, Department of Chemical Engineering, Technion–Israel Institute of Technology, Haifa 32000, Israel

Yael Shammai – Laboratory for Targeted Drug Delivery and Personalized Medicine Technologies, Department of Chemical Engineering, Technion–Israel Institute of Technology, Haifa 32000, Israel

Maya Kaduri – Laboratory for Targeted Drug Delivery and Personalized Medicine Technologies, Department of Chemical Engineering, Technion–Israel Institute of Technology, Haifa 32000, Israel

Lilach Koren – Laboratory for Targeted Drug Delivery and Personalized Medicine Technologies, Department of Chemical Engineering, Technion–Israel Institute of Technology, Haifa 32000, Israel

Omer Adir – Laboratory for Targeted Drug Delivery and Personalized Medicine Technologies, Department of Chemical Engineering, Technion–Israel Institute of Technology, Haifa 32000, Israel; The Norman Seiden Multidisciplinary Program for Nanoscience and Nanotechnology, Technion–Israel Institute of Technology, Haifa 32000, Israel

Jeny Shklover – Laboratory for Targeted Drug Delivery and Personalized Medicine Technologies, Department of Chemical Engineering, Technion–Israel Institute of Technology, Haifa 32000, Israel

Janna Shainsky-Roitman – Laboratory for Targeted Drug Delivery and Personalized Medicine Technologies, Department of Chemical Engineering, Technion–Israel Institute of Technology, Haifa 32000, Israel

Srinivas Ramishetti – Laboratory of Precision NanoMedicine, Shmunis School for Biomedicine and Cancer Research, George S. Wise Faculty of Life Sciences, Center for Nanoscience and Nanotechnology, Department of Materials Sciences and Engineering, Iby and Aladar Fleischman Faculty of Engineering, and Cancer Biology Research Center, Tel Aviv University, Tel Aviv 69978, Israel

Francis Man – School of Biomedical Engineering & Imaging Sciences, King's College London, London SE1 7EH, U.K.; orcid.org/0000-0002-5076-2180

Rafael T. M. de Rosales – School of Biomedical Engineering & Imaging Sciences, King's College London, London SE1 7EH, U.K.; London Centre for Nanotechnology, King's College London, London WC2R 2LS, U.K.

Dan Peer – Laboratory of Precision NanoMedicine, Shmunis School for Biomedicine and Cancer Research, George S. Wise Faculty of Life Sciences, Center for Nanoscience and Nanotechnology, Department of Materials Sciences and

Engineering, Iby and Aladar Fleischman Faculty of Engineering, and Cancer Biology Research Center, Tel Aviv University, Tel Aviv 69978, Israel; orcid.org/0000-0001-8238-0673

Irit Ben-Aharon – Technion Integrated Cancer Center, Faculty of Medicine, Technion, Haifa 320000, Israel

Complete contact information is available at:
<https://pubs.acs.org/10.1021/acsnano.1c07237>

Author Contributions

*M.P. and P.M.-R. contributed equally to this work.

Author Contributions

All authors have given approval to the final version of the manuscript.

Notes

The authors declare no competing financial interest.

ACKNOWLEDGMENTS

This work was supported by the European Union's Horizon 2020 research and innovation program under the grant agreement no. 680242-ERC [Next-Generation Personalized Diagnostic Nanotechnologies for Predicting Response to Cancer Medicine]; a Phospholipid Research Center grant (ASC-2018-062/1-1); the Israel Science Foundation (1881/21, 1778/13, 1421/17); the Israel Ministry of Science & Technology (3-16963, 3-17418); Ministry of Agriculture & Rural Development, Office of the Chief Scientist (323/19); Israel Innovation Authority for a Nofar grant (67967, 880326), the Israel Ministry of Economy for a Kamin grant (69230, 63379); the Israel Cancer Association (2015-0116); the German-Israeli Foundation for Scientific Research and Development for a GIF Young grant (I-2328-1139.10/2012); the European Union FP-7 IRG Program for a Career Integration grant (908049); the Louis Family Cancer Research Fund, Leventhal 2020 COVID19 Research Fund (ATS #11947); a Mallat Family Foundation grant; The Unger Family Fund; and the Carrie Rosenblatt Foundation for Cancer Research. A.S. acknowledges Alon and Taub Fellowships. Images in this paper were created with BioRender.com and Adobe Illustrator. The authors also acknowledge the support of the Technion Integrated Cancer Center (TICC), the Russell Berrie Nanotechnology Institute, and the Lorry I. Lokey Interdisciplinary Center for Life Sciences & Engineering. M.P. wishes to thank the Israeli Ministry of Science and Technology for the Shulamit Aloni Doctoral Fellowship. O.A. wishes to thank the Miriam and Aaron Gutwirth Memorial Fellowship. M.K. wishes to thank TEVA Pharmaceuticals–NFBI–The National Forum for BioInnovators for a doctoral grant and the Technion Integrated Cancer Center (TICC) Rubinstein scholarship. The SPECT-CT imaging studies were funded by a CRUK Multidisciplinary Project Award [C48390/A21153], the EPSRC program for next generation molecular imaging and therapy with radionuclides [EP/S032789/1], the Wellcome EPSRC Centre for Medical Engineering at King's College London [WT 203148/Z/16/Z], a Wellcome Trust Multiuser Equipment Grant [212885/Z/18/Z], and the National Institute for Health Research (NIHR) Biomedical Research Centre based at Guy's and St Thomas' NHS Foundation Trust and KCL [IS-BRC-1215-20006].

REFERENCES

- (1) Robinson, R. S.; Woad, K. J.; Hammond, A. J.; Laird, M.; Hunter, M. G.; Mann, G. E. Angiogenesis and Vascular Function in the Ovary. *Reproduction* **2009**, *138* (6), 869–881.
- (2) Caligioni, C. S. Assessing Reproductive Status/Stages in Mice. *Curr. Protoc. Neurosci.* **2009**, *48* (1), A.41.1–A.41.8.
- (3) Fraser, H. M.; Lunn, S. F. Regulation and Manipulation of Angiogenesis in the Primate Corpus Luteum. *Reproduction* **2001**, *121* (3), 355–362.
- (4) Reynolds, L. P.; Grazul-Bilska, A. T.; Redmer, D. A. Angiogenesis in the Corpus Luteum. *Endocrine* **2000**, *12* (1), 1–9.
- (5) Weis, S. M.; Cheres, D. A. Pathophysiological Consequences of Vegf-Induced Vascular Permeability. *Nature* **2005**, *437* (7058), 497–504.
- (6) Schädlich, A.; Hoffmann, S.; Mueller, T.; Caysa, H.; Rose, C.; Göpferich, A.; Li, J.; Kuntsche, J.; Mäder, K. Accumulation of Nanocarriers in the Ovary: A Neglected Toxicity Risk? *J. Controlled Release* **2012**, *160* (1), 105–112.
- (7) Hirsjärvi, S.; Sancey, L.; Dufort, S.; Belloche, C.; Vanpouille-Box, C.; Garcion, E.; Coll, J.-L.; Hindré, F.; Benoit, J.-P. Effect of Particle Size on the Biodistribution of Lipid Nanocapsules: Comparison between Nuclear and Fluorescence Imaging and Counting. *Int. J. Pharm.* **2013**, *453* (2), 594–600.
- (8) Yan, J.; Kang, D. D.; Dong, Y. Harnessing Lipid Nanoparticles for Efficient Crispr Delivery. *Biomater. Sci.* **2021**, *9*, 6001.
- (9) Jiménez-Jiménez, C.; Manzano, M.; Vallet-Regí, M. Nanoparticles Coated with Cell Membranes for Biomedical Applications. *Biology* **2020**, *9* (11), 406.
- (10) Nakatsuka, N.; Hasani-Sadrabadi, M. M.; Cheung, K. M.; Young, T. D.; Bahlakeh, G.; Moshaverinia, A.; Weiss, P. S.; Andrews, A. M. Polyserotonin Nanoparticles as Multifunctional Materials for Biomedical Applications. *ACS Nano* **2018**, *12* (5), 4761–4774.
- (11) Haag, R.; Kratz, F. Polymer Therapeutics: Concepts and Applications. *Angew. Chem., Int. Ed.* **2006**, *45* (8), 1198–1215.
- (12) Zahedi, P.; Yoganathan, R.; Piquette-Miller, M.; Allen, C. Recent Advances in Drug Delivery Strategies for Treatment of Ovarian Cancer. *Expert Opin. Drug Delivery* **2012**, *9* (5), 567–583.
- (13) Anselmo, A. C.; Mitragotri, S. Nanoparticles in the Clinic: An Update. *Bioeng. Transl. Med.* **2019**, *4* (3), No. e10143.
- (14) Shapiro, C. L.; Manola, J.; Leboff, M. Ovarian Failure after Adjuvant Chemotherapy Is Associated with Rapid Bone Loss in Women with Early-Stage Breast Cancer. *J. Clin. Oncol.* **2001**, *19* (14), 3306–3311.
- (15) Barkalina, N.; Charalambous, C.; Jones, C.; Coward, K. Nanotechnology in Reproductive Medicine: Emerging Applications of Nanomaterials. *Nanomedicine: Nanotechnology, Biology and Medicine* **2014**, *10* (5), No. e921–e938.
- (16) Lloyd-Parry, O.; Downing, C.; Aleisaie, E.; Jones, C.; Coward, K. Nanomedicine Applications in Women's Health: State of the Art. *Int. J. Nanomed.* **2018**, *13*, 1963.
- (17) N'Dea, S.; Nelson, K. M.; Gleghorn, J. P.; Day, E. S. Design of Nanomaterials for Applications in Maternal/Fetal Medicine. *J. Mater. Chem. B* **2020**, *8*, 6548.
- (18) Ferretti, M. T.; Iulita, M. F.; Cavedo, E.; Chiesa, P. A.; Dimech, A. S.; Chadha, A. S.; Baracchi, F.; Girouard, H.; Misoch, S.; Giacobini, E. Sex Differences in Alzheimer Disease—The Gateway to Precision Medicine. *Nat. Rev. Neurol.* **2018**, *14* (8), 457–469.
- (19) Lai, S. K.; Wang, Y.-Y.; Hida, K.; Cone, R.; Hanes, J. Nanoparticles Reveal That Human Cervicovaginal Mucus Is Riddled with Pores Larger Than Viruses. *Proc. Natl. Acad. Sci. U. S. A.* **2010**, *107* (2), 598–603.
- (20) Ferber, S.; Gonzalez, R. J.; Cryer, A. M.; von Andrian, U. H.; Artzi, N. Immunology-Guided Biomaterial's Design as Mucosal Cancer Vaccine. *Adv. Mater.* **2020**, *32*, 1903847.
- (21) Huang, X.; Chisholm, J.; Zhuang, J.; Xiao, Y.; Duncan, G.; Chen, X.; Suk, J. S.; Hanes, J. Protein Nanocages That Penetrate Airway Mucus and Tumor Tissue. *Proc. Natl. Acad. Sci. U. S. A.* **2017**, *114* (32), E6595–E6602.
- (22) La-Beck, N.; Wu, H.; Infante, J.; Jones, S.; Burris III, H.; Keedy, V.; Kodaira, H.; Ikeda, S.; Ramanathan, R.; Zamboni, W. The Evaluation of Gender on the Pharmacokinetics (Pk) of Pegylated Liposomal Anticancer Agents. *J. Clin. Oncol.* **2010**, *28*, No. e13003.
- (23) Hajipour, M. J.; Aghaverdi, H.; Serpooshan, V.; Vali, H.; Sheibani, S.; Mahmoudi, M. Sex as an Important Factor in Nanomedicine. *Nat. Commun.* **2021**, *12* (1), 1–11.
- (24) Mora-Raimundo, P.; Lozano, D.; Manzano, M.; Vallet-Regí, M. Nanoparticles to Knockdown Osteoporosis-Related Gene and Promote Osteogenic Marker Expression for Osteoporosis Treatment. *ACS Nano* **2019**, *13* (5), 5451–5464.
- (25) Rosenblum, D.; Joshi, N.; Tao, W.; Karp, J. M.; Peer, D. Progress and Challenges Towards Targeted Delivery of Cancer Therapeutics. *Nat. Commun.* **2018**, *9* (1), 1–12.
- (26) Zhong, Y.; Goltsche, K.; Cheng, L.; Xie, F.; Meng, F.; Deng, C.; Zhong, Z.; Haag, R. Hyaluronic Acid-Shelled Acid-Activatable Paclitaxel Prodrug Micelles Effectively Target and Treat Cd44-Overexpressing Human Breast Tumor Xenografts in Vivo. *Biomaterials* **2016**, *84*, 250–261.
- (27) Allen, E. The Oestrous Cycle in the Mouse. *Am. J. Anat.* **1922**, *30* (3), 297–371.
- (28) Tamanini, C.; De Ambrogio, M. Angiogenesis in Developing Follicle and Corpus Luteum. *Reprod. Domest. Anim.* **2004**, *39* (4), 206–216.
- (29) Tsuchiya, Y.; Nakajima, M.; Yokoi, T. Cytochrome P450-Mediated Metabolism of Estrogens and Its Regulation in Human. *Cancer Lett.* **2005**, *227* (2), 115–124.
- (30) Weiss, V. M.; Lucas, H.; Mueller, T.; Chytil, P.; Etrych, T.; Naolou, T.; Kressler, J.; Mäder, K. Intended and Unintended Targeting of Polymeric Nanocarriers: The Case of Modified Poly (Glycerol Adipate) Nanoparticles. *Macromol. Biosci.* **2018**, *18* (1), 1700240.
- (31) Raemdonck, K.; De Smedt, S. C. Lessons in Simplicity That Should Shape the Future of Drug Delivery. *Nat. Biotechnol.* **2015**, *33* (10), 1026–1027.
- (32) Owens, D. E., III; Peppas, N. A. Opsonization, Biodistribution, and Pharmacokinetics of Polymeric Nanoparticles. *Int. J. Pharm.* **2006**, *307* (1), 93–102.
- (33) Russell, D. L.; Robker, R. L. Molecular Mechanisms of Ovulation: Co-Ordination through the Cumulus Complex. *Hum. Repro. Update* **2007**, *13* (3), 289–312.
- (34) Zhou, H.; Ohno, N.; Terada, N.; Saitoh, S.; Fujii, Y.; Ohno, S. Involvement of Follicular Basement Membrane and Vascular Endothelium in Blood–Follicle Barrier Formation of Mice Revealed by 'in Vivo Cryotechnique'. *Reproduction* **2007**, *134* (2), 307–317.
- (35) Barenholz, Y. Shake up the Drug Containers. *Nat. Nanotechnol.* **2012**, *7* (8), 483–484.
- (36) Akinc, A.; Maier, M. A.; Manoharan, M.; Fitzgerald, K.; Jayaraman, M.; Barros, S.; Ansell, S.; Du, X.; Hope, M. J.; Madden, T. D.; Mui, B. L.; Semple, S. C.; Tam, Y. K.; Ciufolini, M.; Witzigmann, D.; Kulkarni, J. A.; van der Meel, R.; Cullis, P. R. The Onpatro Story and the Clinical Translation of Nanomedicines Containing Nucleic Acid-Based Drugs. *Nat. Nanotechnol.* **2019**, *14* (12), 1084–1087.
- (37) Edmonds, S.; Volpe, A.; Shmeeda, H.; Parente-Pereira, A. C.; Radia, R.; Bagaña-Torres, J.; Szanda, I.; Severin, G. W.; Livieratos, L.; Blower, P. J. Exploiting the Metal-Chelating Properties of the Drug Cargo for in Vivo Positron Emission Tomography Imaging of Liposomal Nanomedicines. *ACS Nano* **2016**, *10* (11), 10294–10307.
- (38) Spannuth, W. A.; Sood, A. K.; Coleman, R. L. Angiogenesis as a Strategic Target for Ovarian Cancer Therapy. *Nat. Clin. Pract. Oncol.* **2008**, *5* (4), 194–204.
- (39) Hazzard, T. M.; Stouffer, R. L. Angiogenesis in Ovarian Follicular and Luteal Development. *Best Practice & Research Clinical Obstetrics & Gynaecology* **2000**, *14* (6), 883–900.
- (40) Bar-Joseph, H.; Ben-Aharon, I.; Rizel, S.; Stemmer, S. M.; Tzabari, M.; Shalgi, R. Doxorubicin-Induced Apoptosis in Germinal Vesicle (Gv) Oocytes. *Reprod. Toxicol.* **2010**, *30* (4), 566–572.
- (41) Syrgos, K. N.; Vile, R. G.; Peters, A. M.; Harrington, K. J. Biodistribution and Pharmacokinetics of 111In-Dtpa-Labelled

Pegylated Liposomes after Intraperitoneal Injection. *Acta Oncol.* **2003**, 42 (2), 147–153.

(42) Humphries, C. Luck of the Chromosomes. *Nature* **2014**, 516 (7529), S10.

(43) Leonard, R.; Adamson, D.; Bertelli, G.; Mansi, J.; Yellowlees, A.; Dunlop, J.; Thomas, G.; Coleman, R.; Anderson, R. GnRh Agonist for Protection against Ovarian Toxicity During Chemotherapy for Early Breast Cancer: The Anglo Celtic Group Option Trial. *Ann. Oncol.* **2017**, 28 (8), 1811–1816.

(44) Bedoschi, G.; Turan, V.; Oktay, K. Utility of GnRh-Agonists for Fertility Preservation in Women with Operable Breast Cancer: Is It Protective? *Curr. Breast Cancer Rep.* **2013**, 5 (4), 302–308.

(45) Roness, H.; Kalich-Philosoph, L.; Meiorow, D. Prevention of Chemotherapy-Induced Ovarian Damage: Possible Roles for Hormonal and Non-Hormonal Attenuating Agents. *Hum. Reprod. Update* **2014**, 20 (5), 759–774.

(46) Jemiolo, B.; Harvey, S.; Novotny, M. Promotion of the Whitten Effect in Female Mice by Synthetic Analogs of Male Urinary Constituents. *Proc. Natl. Acad. Sci. U. S. A.* **1986**, 83 (12), 4576–4579.

(47) Byers, S. L.; Wiles, M. V.; Dunn, S. L.; Taft, R. A. Mouse Estrous Cycle Identification Tool and Images. *PloS one* **2012**, 7 (4), No. e35538.

(48) Zinger, A.; Koren, L.; Adir, O.; Poley, M.; Alyan, M.; Yaari, Z.; Noor, N.; Krinsky, N.; Simon, A.; Gibori, H. Collagenase Nanoparticles Enhance the Penetration of Drugs into Pancreatic Tumors. *ACS Nano* **2019**, 13 (10), 11008–11021.

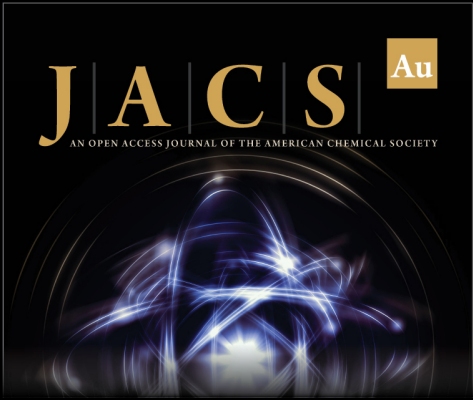
(49) Ramishetti, S.; Hazan-Halevy, I.; Palakuri, R.; Chatterjee, S.; Naidu Gonna, S.; Dammes, N.; Freilich, I.; Kolik Shmuel, L.; Danino, D.; Peer, D. A Combinatorial Library of Lipid Nanoparticles for Rna Delivery to Leukocytes. *Adv. Mater.* **2020**, 32 (12), 1906128.

(50) Haran, G.; Cohen, R.; Bar, L. K.; Barenholz, Y. Transmembrane Ammonium Sulfate Gradients in Liposomes Produce Efficient and Stable Entrapment of Amphipathic Weak Bases. *Biochimica et Biophysica Acta (BBA)-Biomembranes* **1993**, 1151 (2), 201–215.

(51) Arroyo-Crespo, J. J.; Armiñán, A.; Charbonnier, D.; Deladriere, C.; Palomino-Schätzlein, M.; Lamas-Domingo, R.; Forteza, J.; Pineda-Lucena, A.; Vicent, M. J. Characterization of Triple-Negative Breast Cancer Preclinical Models Provides Functional Evidence of Metastatic Progression. *Int. J. Cancer* **2019**, 145 (8), 2267–2281.

(52) Shmeeda, H.; Amitay, Y.; Gorin, J.; Tzemach, D.; Mak, L.; Stern, S. T.; Barenholz, Y.; Gabizon, A. Coencapsulation of Alendronate and Doxorubicin in Pegylated Liposomes: A Novel Formulation for Chemoimmunotherapy of Cancer. *J. Drug Targeting* **2016**, 24 (9), 878–889.

(53) Volpe, A.; Man, F.; Lim, L.; Khoshnevisan, A.; Blower, J.; Blower, P. J.; Fruhwirth, G. O. Radionuclide-Fluorescence Reporter Gene Imaging to Track Tumor Progression in Rodent Tumor Models. *J. Visualized Exp.* **2018**, No. 133, No. e57088.



JACS Au
AN OPEN ACCESS JOURNAL OF THE AMERICAN CHEMICAL SOCIETY

Editor-in-Chief
Prof. Christopher W. Jones
Georgia Institute of Technology, USA

Open for Submissions

pubs.acs.org/jacsau

ACS Publications
Most Trusted. Most Cited. Most Read.